RSC Advances

ROYAL SOCIETY OF CHEMISTRY

www.rsc.org/advances

Combustion deposition of MoO_3 films: from fundamentals to OPV applications

Wouter Marchal[1], Christopher De Dobbelaere[1], Jurgen Kesters[2], Gilles Bonneux[1], Joke Vandenbergh[2], Hanne Damm[1], Thomas Junkers[2,3], Wouter Maes[2,3], Jan D'Haen[3,4], Marlies K. Van Bael[1,3], An Hardy[1,3*]

1. Hasselt University, Institute for Materials Research, Inorganic and Physical chemistry, Martelarenlaan 42, 3500 Hasselt, Belgium

2. Hasselt University, Institute for Materials Research, Organic and Bio-polymer chemistry, Martelarenlaan 42, 3500 Hasselt, Belgium

3. IMEC vzw, division IMOMEC, Agoralaan Building D, 3590 Diepenbeek, Belgium

4. Hasselt University, Institute for Materials Research, Materials Physics, Martelarenlaan 42, 3500 Hasselt, Belgium

Combustion – organic photovoltaics – Molybdenum oxide – Thermal analysis – hole transporting layer

Abstract

A systematic study of a combustion precursor's thermal decomposition pathway is undertaken, in both powders and thin films, to obtain insights in the various parameters influencing the combustion process. The study focuses on MoO_3 as a hole transporting layer (HTL) for applications in organic photovoltaics (OPV). Via evolved gas analysis, it was found that fuel volatility occurs prior to the actual combustion reaction of the acetylacetonate based precursor, affecting the optimal oxidizer to fuel ratio. Moreover, close investigation showed that the high rate combustion reaction disappears with increasing surface to volume ratio. Nonetheless, thermal analysis performed on films suggests that with the right heating rate, an oxidative complete decomposition still occurs in films, exemplified by the film composition and specific morphological differences in the resulting layers and through analysis of the evolved components. Finally, the discussed synthesis route allows to obtain organic free, crystalline MoO_3 films affording organic solar cell devices with promising current density-voltage characteristics.

Introduction

Combustion synthesis is a well-documented synthesis route that allows to obtain a wide variety of tailor-made oxide powders [1-4]. In this paper, combustion is referred to as a self-sustainable oxidative reaction mechanism initiated by the presence of nitrates. The locally initiated combustion heat is propagated throughout the material, continuously consuming the reactants and eventually leading to a thermal runaway process [5, 6]. By influencing and controlling this thermal effect, the required energy for formation of the desired oxide phase can be generated without the need for subsequent high temperature calcination steps. Various types of combustion based synthesis mechanisms are reported in literature such as sol-gel combustion [1], solution combustion [7] including volume combustion synthesis and self-propagating high-temperature synthesis [8] and smoldering [9]. Generally, there are three requirements for a combustion process: heat to trigger the in-situ exothermic reaction, a fuel with a high combustion enthalpy and an oxidizer. If the oxidizer, mostly a nitrate salt, is present inside the precursor system, the thermal process is often referred to as auto-combustion [10]. In an optimized system, fuel and oxidizer are present in a stoichiometrically balanced composition [11, 12] to reach the maximal adiabatic temperature and thereby the highest reaction exothermicity [13].

Besides the low temperature synthesis of powders, the process also holds promise [14] for film synthesis on temperature-sensitive substrates, such as flexible plastics. However, the topic of combustion synthesis in films is currently strongly debated in literature [15-17]. An in situ heating reaction mechanism in films is far from evident. Indeed, to initiate a thermal runaway effect, the heat generation rate has to be higher than the heat dissipation rate. The proportion between both rates strongly depends on the surface to volume ratio of the material [18]. Since films with nanoscale thickness have a relatively high surface area compared to their volume, the propagation of the combustion front in nanometer-scale films is questioned [15]. This study contributes to the debate by providing experimental evidence for the particular case of MoO_3 films, keeping in mind the aforementioned considerations regarding the internal heating. More specific, the effect of the evaporation of the presented components is extensively elaborated upon.

In order to determine whether combustion synthesis can be used to obtain functional thin films at low temperatures, oxide layers were synthesized for their application as hole transporting materials in organic photovoltaics (OPV's). One of the major prerequisites for the commercial viability of this technology is the printability of the functional materials on (plastic) flexible substrates using cheap techniques such as solution processing [19]. As such, through judicious scientific efforts, MoO_3, V_2O_5 and WO_3 were pushed forward as potential candidates for use as transparent metal oxide (TMO) interfacial layers [20]. These n-type semiconductor materials reduce the energy barrier for hole transport at the anodic interface, due to an excellent energy level

alignment between the TMO and the organic photoactive layer [21]. The exact stoichiometry and the specific oxidation state of molybdenum are important to obtain a functional molybdenum oxide hole transporting layer [22]. Therefore, MoO_3 has already been implemented in various device stacks yielding a wide range of PCE values depending on the processing and device stack (solution processed MoO_3: 2.5 – 3.5 %, evaporated MoO_3: 4.9 – 6.3 %) [23]. Up to now, WO_3 and V_2O_5 are explored to a lower extent, but also hold promise as PCE values of 3.4 % and 3 % were reported respectively [24, 25]. Moreover, MoS_2-MoO_3 double layer HTL's are currently explored, reaching PCE values up to 4.15 % due to the presence of Mo^{5+} and Mo^{6+} states in the MoS_2 layer, causing p-type conductive behavior [26]. Alternatively, various TMO's are also implemented as electron conducting layers such as ZnO and TiO_2 [27], showing once more the possible synergy between 'inorganic ceramic' TMO's and the polymer based active materials.

The major advantages of MoO_3 as hole transporting layer, in contrast to PEDOT:PSS, a regularly used organic (polymeric) alternative, are its long-term stability [28], non-toxic nature, high shunt resistance [29] and deep lying electronic states [30]. Functional MoO_3 layers have already been obtained by a wide variety of deposition techniques such as thermal evaporation [30, 31], chemical vapor deposition [32], electron gun deposition [33], pulsed laser deposition [34] and chemical solution deposition such as electrodeposition [35] and spin coating from suspension or solution [36, 37]. Though the pricing of the employed solvents and reagents plays a role, in general, chemical solution deposition is presented as a cost-effective way to produce a wide range of high quality electronic oxide thin films [38] which has potential for scalability toward commercial production (also in OPV context) [39]. In the present work, standard alcohols are employed in ambient conditions, providing the opportunity for low-cost processing.

Although the aforementioned deposition techniques work well, combustion synthesis can offer some additional benefits. It is an elegant way for the facile introduction of dopants (inherent to solution processing) and crystalline layers can be obtained at a low temperature compared to other deposition techniques [40-42], aspiring compatibility with temperature-sensitive substrates such as polyimide substrates. Both features are considered in literature to promote the electrical conductivity of molybdenum oxide layers [43, 44] and to compensate the elevated series resistance, reducing the J_{sc} if the layer thickness exceeds 50 nm [29]. Both the enhanced crystallinity [43] and a proper choice of the dopants are believed to have a beneficial influence on the OPV device performance.

In this article, powder combustion of MoO_3 is studied with respect to the influence of the oxidizer/fuel ratio, the surface to volume ratio and the heating rate. Based on the principal role of fuel (and in some cases oxidizer)

evaporation, the decomposition mechanism resulting in molybdenum oxide films is critically evaluated, with a specific focus on the dimensions of the system. Using the synthesis route presented, flexibility to introduce extra dopants is acquired and crystalline MoO_3 layers can be obtained.

Experimental

Precursor chemistry

Molybdenum(VI)oxide bis(2,4-pentanedione) (99%, Alfa Aesar) and ammonium nitrate (extra pure, >98.5 % Merck) were used as received. Molybdenum precursor solutions of 0.05 M, 0.10 M, 0.20 M and 0.30 M were prepared in methanol (>99.9 %, Acros Organics). These reagents were added to methanol in the desired concentration and magnetically stirred until dissolution. Various oxidizer (nitrate)/fuel (acetylacetonate) ratios were prepared to identify the optimal composition for combustion. The molecular species in solution were studied with soft electro spray ionization mass spectrometry (ESI-MS) measurements using an LTQ Orbitrap Velos Pro mass spectrometer (ThermoFischer Scientific) equipped with an atmospheric pressure ionization source operating in the nebulizer assisted electrospray mode. The instrument was calibrated in the m/z range 220−2000 using a standard solution containing caffeine, MRFA, and Ultramark 1621. A constant spray voltage of 3.5 kV was used, and nitrogen at a dimensionless sheath gas flow rate of 8 was applied. The S-lens RF level, the gate lens voltage, the front lens voltage and the capillary temperature were set to 50%, −90 V, −8.5 V, and 275 °C, respectively. A 250 µL aliquot of a MoO_3 solution with a concentration of 0.1 mM was injected. Methanol HPLC grade (VWR) was used as solvent.

Thermal analysis

Thermogravimetric analysis was performed on both powders and films. Powders were obtained by drying the different molybdenum precursors in a Petri dish on a hotplate (Präzitherm, TR 28-3T) for 2 hours in a temperature range of 45–60 °C, evaporating the methanol solvent. Subsequently, the obtained residue was sieved using a vertical sieve column consisting of several levels to separate various size fractions. The isolated powder fraction diameters range from > 2 mm, 2–1 mm, 1000–710 µm, 710–400 µm, 400–125 µm, 125–63 µm and < 63

µm. To obtain fractions of the smallest size, a supplementary grinding step was performed on part of the dried precursor before sieving.

Films for thermal analysis were obtained by spin coating (POLOS wafer spinner) a molybdenum containing precursor (0.2 M) on circular 6 mm diameter borosilicate covering glass (VWR Micro Cover Glasses, thickness 0.08 mm). The covering glasses were soft cleaned by 10 minute sonication steps in respectively Milli-Q water, acetone (VWR, technical) and isopropanol (Merck, for analysis). Subsequently, 30 minutes of UV-ozone treatment (Novascan PSD pro series) was applied at 60 °C to remove organic contamination and improve wettability. The spin coating processing parameters were 500 rpm for 60 seconds (acceleration: 1000 rpm/s) and subsequently 1500 rpm for 60 seconds (1000 rpm/s). This slow rotation speed assured that sufficient material was deposited onto the cover glass surface, taking into account the sensitivity for the EGA (evolved gas analysis). This resulted in a film with an approximate mean thickness of 0.31 micron (Figure S1). Additionally, the film was dried for 2 minutes at 60 °C on a hotplate. Prior to precursor deposition, the covering glasses were weighed in the TG-MS setup (TA instruments Q 5000) with the same gas flow parameters (25 ml/min dry air) and sample pans (High-T Pt) as during the TG-MS measurements to reduce systematic errors. The TG-MS measurements were performed by introducing the coated covering glass in the TG-MS and the weight of the blank substrate was subtracted resulting in sample masses of 0.2-0.3 mg.

Powders were analyzed in a TA instruments SDT Q 600 (TGA-DTA) in dry air using alumina 90 µl cups, applying a heating rate of 10 °C/min in dry air, unless stated otherwise. The evolved gas analysis was performed via TG-MS (TA instruments TGA Q 5000, Pfeiffer quadrupole MS, High-T Pt sample pan) and TG-FTIR (Mettler-Toledo TGA/DSC 1 coupled to a Bruker Vertex 70, alumina 70 µl cup). TG-MS measurements yield ion currents for all the selected m/z values (range, time scan) and time-resolved infrared spectra could be obtained via TG-FTIR, complemented by Gram-Schmidt plots integrating all the signals in a selected wavenumber range. After analysis, the remaining powder was dispersed in a KBr pellet (0.2 mass %) and analyzed by means of FTIR (Bruker Vertex 70, 32 scans, scan range 4000–400 cm^{-1}, resolution 4 cm^{-1}) at room temperature.

MoO_3 film deposition and characterization

Molybdenum oxide films were deposited on both soft cleaned (vide supra) Si/SiO_2 (1.2 nm) native oxide and patterned ITO coated glass substrates (Kintec, 100 nm, 20 Ohm/sq) by spin coating (3000 rpm, 30 seconds, 1000 rpm/s). The same processing parameters were used for the MoO_3 films in the OPV devices. The as-deposited films were subsequently dried on a hotplate at 60–80 °C and then subjected to a higher hotplate temperature (200–300 °C) to induce MoO_3 formation. Moreover, an extra calcination step (at 300 °C), applied after the complete deposition of all layers, was often required to remove organic char and promote the desired phase. These post-hotplate steps were performed in a RTP setup (Annealsys, AS-One) for maximum temperature and atmosphere control.

Infrared spectra of the obtained films were acquired by performing grazing incidence attenuated total reflection FTIR (GATR-FTIR) via a 65° single reflection Ge-ATR Harrick crystal, an accessory inserted into the Bruker Vertex 70 spectrometer (4000–600 cm^{-1}, 36 scans, resolution 4 cm^{-1}, torque: 56 ounce/inch). Raman analysis was carried out on a Horiba Jobin Yvon T64000 in subtractive backscattering mode with a 488 nm laser and a monochromator operating in double subtraction mode. The power of the laser was intentionally reduced to 1.2 mW to avoid phase formation by sample heating during the measurement, which is a well-known phenomenon for amorphous MoO_3 layers [45]. Crystalline phases were identified by X-ray diffraction using a Siemens D-5000 diffractometer with Cu-Kα1 radiation. The morphology was characterized by SEM (scanning electron microscopy, FEI Quanta 200 FEG-SEM), equipped with secondary- and back-scattered electron detectors. Transparency measurements were conducted with the Cary 5000 UV-Vis-NIR spectrometer (Agilent technologies) in scan mode with a dedicated sample holder for films. The borosilicate glass and ITO background were subtracted (Zero/baseline correction) which means the displayed data only relate to the MoO_3 layers.

OPV processing and characterization

Bulk heterojunction (BHJ) organic solar cells were fabricated by stacking the following layers: glass/ITO/MoO_3/PCDTBT:$PC_{70}BM$/Ca/Al. Before deposition of the molybdenum oxide layer by spin coating, the ITO coated substrates (Kintec, 100 nm, 20 Ohm/sq) were soft cleaned (vide supra). After applying the molybdenum oxide (layer thickness ≈ 30 nm) layer, further processing was continued in a nitrogen containing glovebox (O_2/H_2O < 1 ppm), starting with the deposition of the photoactive layer, consisting of PCDTBT (poly[[9-(1-octylnonyl)-9*H*-carbazole-2,7-diyl]-2,5-thiophenediyl-2,1,3-benzothiadiazole-4,7-diyl-2,5-thiophenediyl]; Solarischem) and $PC_{70}BM$ ([6,6]-phenyl-C_{70}-butyric acid methyl ester; Solenne) in a 1:4

(wt/wt%) ratio with a 20 mg/mL total concentration and by using *ortho*-dichlorobenzene (Sigma Aldrich) as the processing solvent. As such, a final active layer thickness of 60–80 nm was procured. Finally, the 30 nm Ca and 80 nm Al top electrodes were deposited by vacuum evaporation, completing the stack with an active area of 3 mm^2. The OPV output characteristics were measured using a Newport class A solar simulator (model 91195A) calibrated with a silicon solar cell, yielding an AM 1.5 G spectrum.

Results and discussion

The molybdenum precursor described in the experimental section is analyzed by means of ESI-MS (Figure 1) to gain insights on the present chemical species, which may differ from the added reactants. Indeed, Grybos *et al.* [46] reported partial Hacac evolution in methanol solutions of vanadyl acetylacetone $VO(acac)_2$, with a structure strongly related to $MoO_2(acac)_2$, caused by methoxy and hydroxyl fragments replacing the acetylacetonate ligand. Similar behavior for our $MoO_2(acac)_2$ system in methanol is confirmed by ESI-MS measurements. The patterns in the ESI-MS (Figure 1) measurement can be linked to the abundances of molybdenum isotopes. By taking into account the mass of the present organic fragments, the molybdenum-containing coordination compounds can be reconstructed, based on literature reports [20].

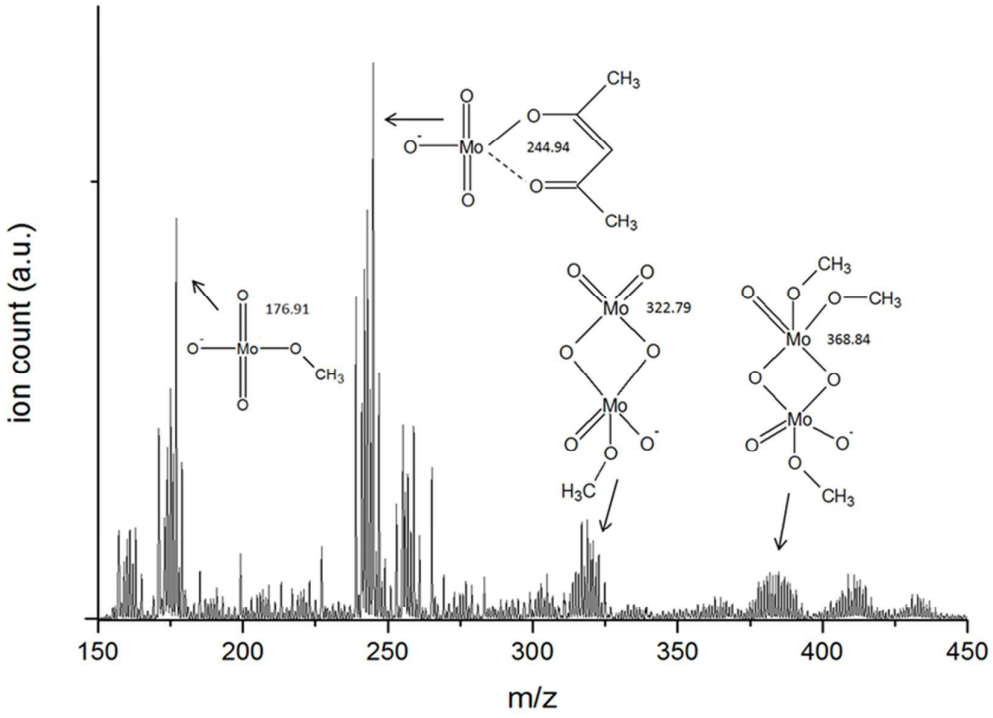

Figure 1. Negative electrospray ionization mass spectra of the $MoO_2(acac)_2$ precursor in methanol showing the existing entities in solution [20] using the ^{98}Mo nucleus to calculate the molecular masses. Detailed information on the species identification can be found in Figure S2.

A. Oxidizer/Fuel ratio

In order to obtain an optimal combustion reaction (highest theoretical adiabatic temperature), an oxidizer/fuel equivalence ratio of 1 is generally required, in accordance with a stoichiometric reaction mixture [47]. By summing all the oxidizing and reducing valences, this equivalence can be calculated [11, 47] presuming that the reaction products are only H_2O, CO_2 and N_2, and no loss of reagents via alternative mechanisms occurs. This method is used by the majority of the authors reporting on combustion synthesis [48-51]. The coordinated 2,4-pentanedionate (often referred to as acetylacetonate or $acac^-$) ligands provide the fuel which releases energy upon oxidation by the present nitrate ions. In the studied system, ammonium nitrate is added to oxidize the acetylacetonate fuel, which allows to postulate the following combustion reaction.

$$MoO_2(C_5H_7O_2)_2 + 24\,NH_4NO_3 \rightarrow 10\,CO_2 + 55\,H_2O + 24\,N_2 + \ MoO_3 \quad (1)$$

From now on, the molar ratio is used to discuss the relative presence of oxidizer and fuel to avoid confusion with the equivalence ratio. The reaction indicates a molar [$NH_4NO_3/C_5H_7O_2$] ratio of 12 to be optimal. However, this was not supported by TGA/DTA experiments carried out on precursors containing different oxidizer/fuel ratios. A thermal runaway reaction associated with an ideal combustion can be recognized as a sudden, strong exothermic reaction which decomposes the organic fuel in a single step [17, 52]. TGA measurements performed in a N_2 atmosphere indicate a similar sudden mass loss, which clearly points to a combustion reaction caused by the present nitrates (Figure S3). As illustrated by the TG profiles of various oxidizer/fuel ratios (Figure 2), a molar (NO_3^- oxidizer/ $acac^-$ fuel) ratio of 0.5 seems to be favorable as the decomposition occurs in only one step, removing all the organic fuel at once for a size fraction of 1-2 mm. In contrast to the theoretical predictions, this strongly diverging ratio is justified since not only CO_2, N_2 and H_2O are evolving during decomposition, as supported by the TG-FTIR results (vide infra) and because of a mechanism of ligand exchange, further elaborated below. The theoretical residual masses for an oxidizer/fuel ratio of 2, 1 and 0.5 are 22.08 %, 29.46 % and 35.34 % respectively, presuming formation of MoO_3. However, slightly higher residual masses were experimentally found at 400 °C, attributable to the evaporation of volatile components at the drying step of 60 °C and to the fact that some organic remainders are only burned between 400 °C and 500 °C (Figure S3, Figure S4). The drying step temperature of the precursor powder prior to the TGA influences the residual mass at 400 °C, which can be rationalized by a ligand exchange process, as no influence on the powder composition is observed (FTIR, Figure S5). The organic residue may have a negative influence on the eventual film conductivity.

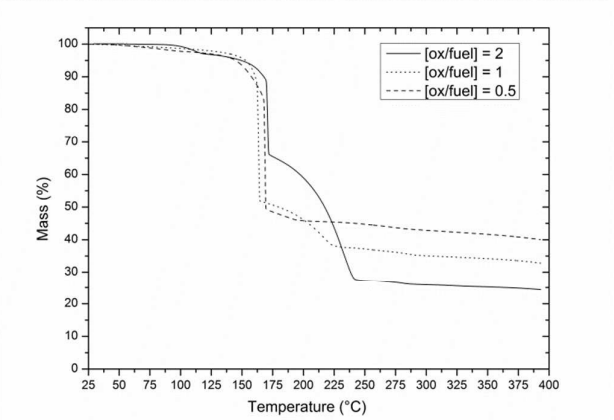

Figure 2. TG profiles (10°C/min) for various molar oxidizer/fuel ratios on 1-2 mm grains. The contribution of the steep combustion related mass decrease around 165 °C gradually becomes less important if the oxidizer fuel ratio becomes higher.

This deviating oxidizer/fuel ratio is further explored by Gram-Schmidt plots of the evolved components (Figure 3). In case of a 0.5 oxidizer/fuel ratio, almost all volatile components evolve in a single step, pointing to an ideal combustion reaction, resulting in a quasi-horizontal Gram-Schmidt baseline after 200 °C. However, the non-zero signal after 200 °C indicates small weight losses originating from the combustion of residual carbon (CO and CO_2 signals), water and ammonia (FTIR based evolved gas analysis, Figure S6). If more nitrates are added (molar oxidizer/fuel ratio of 1 and 2), the reaction pathway changes and additional decomposition steps are explained by the presence of excess nitrate ions (Figure 2 and Figure 3). The precursor systems with oxidizer/fuel ratios of 0.5 and 1 exhibit a sharp signal between 160 and 170 °C corresponding to the combustion step, releasing CO_2 and CO gasses (inset Figure 3). However, online FTIR spectra of the components released during the Gram-Schmidt peak (inset Figure 3) indicate that a substantial amount of acetylacetone (Hacac) is evolving from the sample, proving that part of the fuel evaporates prior to or during the oxidative decomposition, which will have consequences on the ideal oxidizer/fuel ratio. This observation can be perfectly rationalized by the ligand exchange illustrated in the ESI-MS (Figure 1). The released acetylacetone will be evaporated when approaching its boiling point of 140 °C. This partial evaporation process of Hacac elucidates the deviation of the optimal oxidizer/fuel ratio for this precursor system. As part of the Hacac is already evaporated before it can take part in the expected combustion reaction, a substantially lower amount of oxidizer will be required.

An important observation on the optimal nitrate content study is the fact that the oxidizer/fuel ratio corresponding to an ideal single-step decomposition at low temperature is depending on the surface to volume ratio of the powder or film. The changing surface area influences the relative contribution of both Hacac evaporation and non-oxidative nitrate decomposition (vide infra).

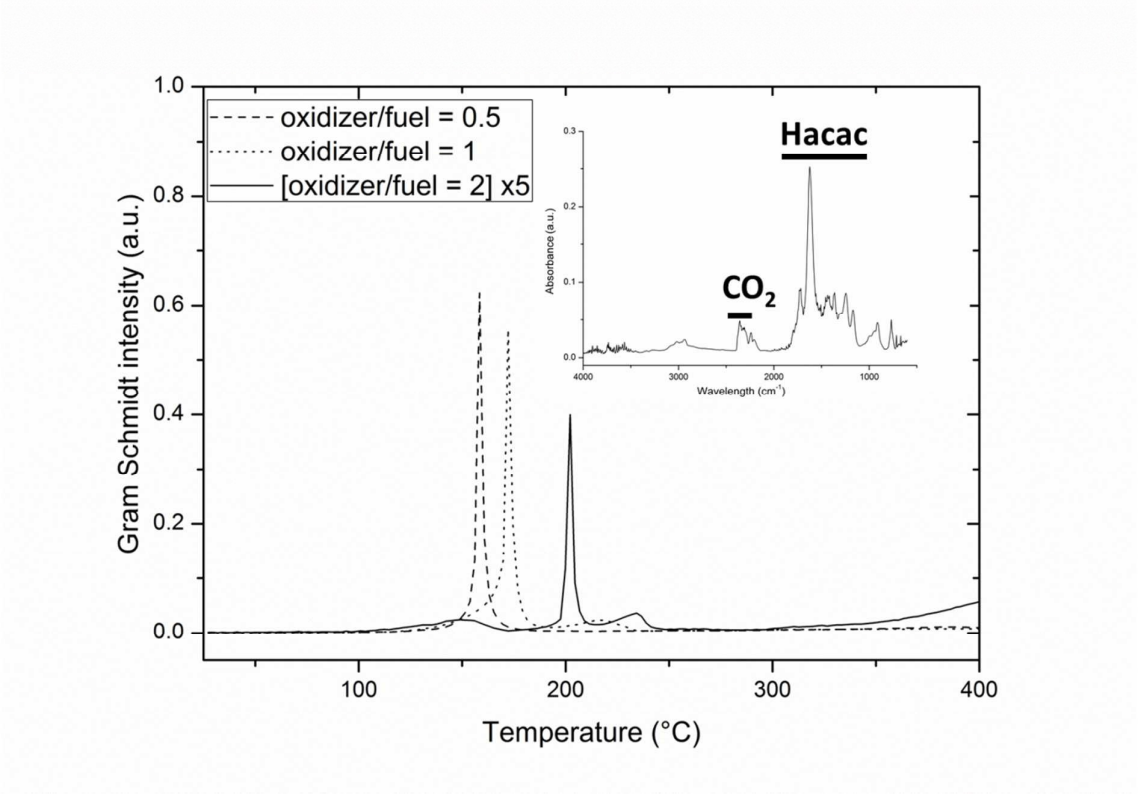

Figure 3. Gram-Schmidt plots of various reaction mixtures on a temperature scale corresponding to the TG profiles in Figure 1. The solid line corresponding to an oxidizer/fuel ratio = 2 is multiplied by 5 to match the ordinate scale. Inset: EGA-FTIR spectrum at 160 °C for an oxidizer/fuel ratio of 1.Gram-Schmidt plots illustrate the change in overall spectral intensity during the TG-FTIR measurement (integrated between 600 and 4000 cm^{-1}, with background subtraction at room temperature) as a function of temperature.

B. Surface/volume ratio

The difference in thermal behavior regarding decomposition and possible combustion for ceramic films compared to powders [53] is clearly shown by Sanchez-Rodriguez *et al.* [15]. To attain a self-sustaining exothermic reaction, sufficient powder volume is necessary and heat dissipation should be constrained by limiting the free surface area, as calculated from physicochemical equations suggested by Narendar *et al.* [18] and Yi *et al* [53]. Here, this effect is quantified by sieving the dried combustible precursor powder into various size fractions, implying higher surface to volume ratios for smaller grain sizes. Figure 4a shows the thermal decomposition profiles of the different size fractions using approximately the same sample mass for every measurement. The profile is marked at different temperatures (I, II, III) for which the evolving gases are presented in Figure 5.

The combustion step (Figure 4a (I)) is associated with a strong sudden mass decrease around 165-170 °C (variation of ± 5 °C between different measurements). The thermal profile clearly indicates the influence of the

size fraction on the combustion behavior. Whereas size fractions of 2-1 mm and 1000-710 µm show a strong and violent combustion reaction, the smaller fractions decompose in a more gradual fashion. Furthermore, the thermal profiles of the larger size fractions exhibit a distinct supplementary decomposition step after the combustion (Figure 4a between (I) and (II)). This is due to the non-oxidative decomposition of the excess ammonium nitrate, as the oxidizer/fuel ratio is not optimal in this system (NH_4NO_3/$acac^-$ ratio = 1). Eventually, unburned carbon fragments can be oxidized by residual nitrates in a successive reaction stage (Figure 4a (III)), identified by the characteristic evolved gaseous components N_2O and NO_2. Each reaction stage will be described more into detail in the following paragraphs.

The pronounced exothermic differential thermal analysis (DTA) signal corresponding to the main weight loss step at 170 °C delivers additional evidence on the observed trends in the combustion reaction (Figure 4b). In the previous section, the evaporation of Hacac was demonstrated in the same temperature range. However, as the DTA signal is the sum of all occurring phenomena, the pronounced exothermic signal in the short time span between 160 °C and 185 °C of the overall reaction is even stronger evidence of the presence of a significant combustion step. The pronounced exothermic signal is gradually fading out by diminishing the powder grain size. This trend indicates that the higher surface to volume ratio inhibits the thermal runaway effect (no autocombustion). For small powder fractions, the weight loss is caused by fuel evaporation (for 63 µm size fractions, almost no CO_2 evolution is observed in the EGA, Figure 5a) making low temperature film synthesis still possible due to Hacac evaporation (boiling point = 140°C).

Moreover, for nano sized thin films, the surface to volume ratio is even much higher. Given the simplification of a perfectly flat and round film with a thickness of 0.30 µm (approximate thickness of one layer, determined by cross section SEM, Figure S1), and a diameter of 6 mm, the surface to volume ratio of such a film is 66.6×10^5 m^{-1}, whereas this ratio is approximately 95.2×10^3 m^{-1} for spherical particles with a diameter below 63 micron. The surface of the film is defined as the interface between the molybdenum containing coating and both the ambient atmosphere and the underlying substrate. This calculation (which is not considering the difference in heat dissipation factors via the substrate and the ambient atmosphere) illustrates that if these TGA results are extrapolated to films, an even smaller contribution of the combustion reaction to the total thermal decomposition of the film can be expected.

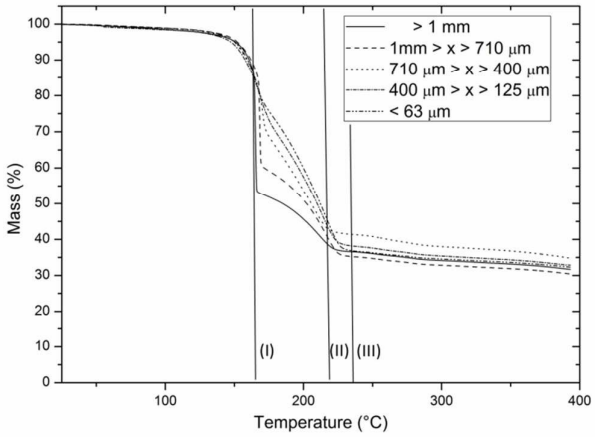

Figure 4a. Thermal decomposition profile of various size fractions at a heating rate of 10 °C/min with [NO_3^-/$acac^-$] = 1, establishing the powder size effect on combustion. Average sample weight: 3.562 mg, corrected sample standard deviation: 0.1273 mg. The reproducibility of the TGA analysis is briefly illustrated in Figure S8.

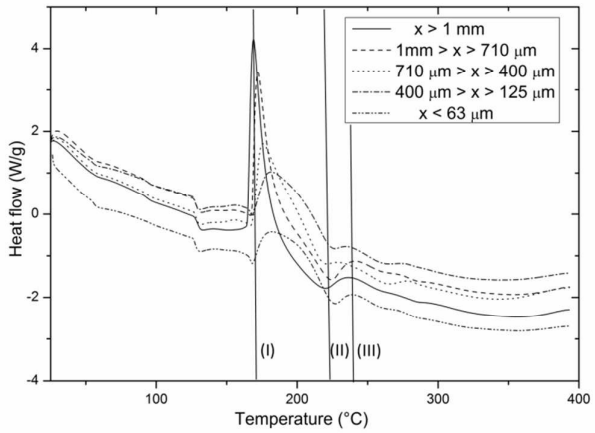

Figure 4b. DTA signals corresponding to the thermal decomposition profiles (recorded by simultaneous TGA-DTA), indicating the evolution of the combustion reaction exothermicity in case of varying size fractions. The small endothermic signals around 125 °C and 160 °C correspond to a polymorph transformation and the melting of ammonium nitrate, respectively. Exothermic phenomena are depicted by upward signals.

The exothermic combustion signal is followed by a gradually decreasing heat flow reaching a minimum around 220 °C (Figure 4a (II), 4b), corresponding to the endothermic evaporation of excess nitrates (Figure 5b, 5c, reaction 2 and 3). The small exothermic signal at 240 °C points to the oxidative removal of residual organics (proven by the identity of the evolved components corresponding to exothermic interaction [2], Figure 5c). Eventually, the slightly decreasing baseline indicates further removal of organics and other volatile components which are identified further in this paper.

Upon decreasing the particle size, the release of volatile components, detected by online coupled MS and FTIR, occurs less concentrated, illustrated by the more gradual weight loss in Figure 4a. The most important ions observed in mass spectrometry at temperatures around 160 °C are listed in Table 1. From these fragments, it is clear that the mass loss originates from mixed processes: the release of N_2 (only from MS, since it is IR inactive), NO, H_2O, CO and CO_2 points to the combustion of the acetylacetonate fuel, whereas fragments such as 15, 42, 43 and 85 m/z indicate α-cleavage of free acetylacetone, released by evaporation. When the powder's grain size is reduced, the contribution of the combustion reaction to the total decomposition lowers. Hardly any CO_2 evolution can be observed for the 63 µm size fraction, whereas the IR spectrum of the 2 mm fraction clearly indicates the fuel decomposition into CO and CO_2 (Figure 5a). This observation can be explained by the significant heat dissipation of the 63 µm fraction, caused by the larger surface to volume ratio, inhibiting the combustion process and enhancing the acetylacetone evaporation prior to combustion.

Table 1. Overview of detected mass ions originating from evolved gasses in online TG-MS analysis at 163 °C, corresponding with the main mass loss in the profile. The identified ions indicate the occurrence of both combustion and evaporation.

163 °C	
Observed ions	Evolved gas
14 (N^+) 28 (N_2^+) (CO^+)	N_2 and CO
17 (OH^+)(NH_3^+) 18 (H_2O^+)	H_2O and NH_3
44 ($C^{12}O_2^+$) 45($C^{13}O_2^+$)	CO_2
15(CH_3^+) 42 ($OCCH_2^+$) 43 ($OCCH_3^+$) 85 ($CH_3COCH_2CO^+$) 100 ($CH_3COCH_2COCH_3^+$)	Hacac
30 (NO^+)	NO

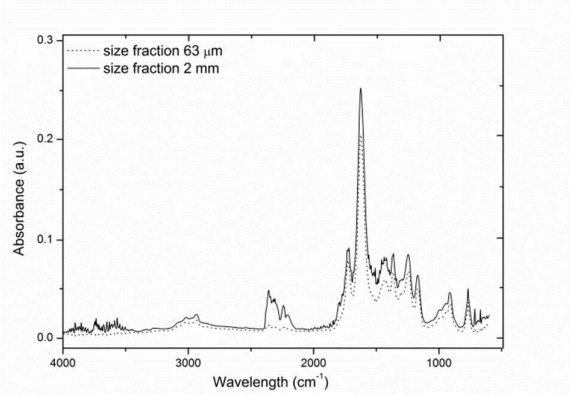

Figure 5a. Infrared spectra of different powder size fractions at 160 °C. 2358 cm^{-1} (vs) CO_2, doublet 2240 and 2205 cm^{-1} (s) CO, 1718 and 1628 cm^{-1} correspond to the C-O vibration of the keto and enol tautomer of acetylacetone, respectively. The other signals below 1500 cm^{-1} can all be assigned to the acetylacetone fragment.

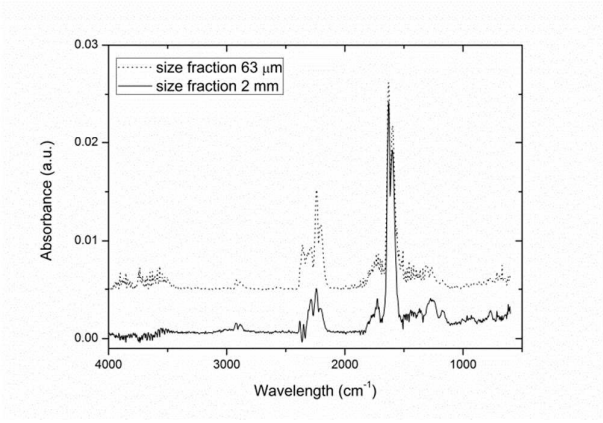

Figure 5b. Infrared spectra of different powder size fractions at 220 °C. Both spectra clearly contain traces of NO_2 and water evolution. H_2O: rotational fine structure signals above 3500 cm^{-1} and around 1600 cm^{-1}, NO_2 doublets at 1610 cm^{-1}(vs) and 2905 cm^{-1}(m). The 63 μm spectrum also contains evidence for N_2O evolution. This oxidative process will reach its maximum at slightly higher temperatures, however there is some overlap between both processes. Signals are normalized to sample size.

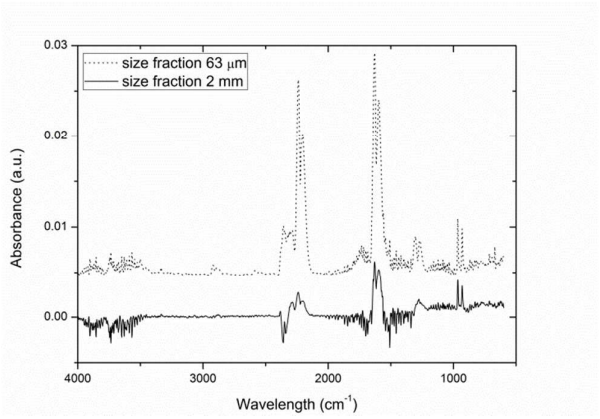

Figure 5c. Infrared spectra of different powder size fractions at 240 °C. The 2 mm fraction shows the aftermath of the nitrate evaporation. In contrast, the 63 μm fraction spectrum clearly shows the development of N_2O gas, proved by the doublets at 2220 cm^{-1} (vs) and 1285 cm^{-1} (m). Although the 2220 cm^{-1} signal also corresponds to CO, the doublet at 1285 cm^{-1} is very distinctive for N_2O. In both spectra, the evaporation of ammonia can be observed as well, as seen by the doublet around 950 cm^{-1}. Signals are normalized to sample size.

Although the previous section on the oxidizer/fuel ratio showed that a molar ratio of 0.5 corresponded to the most efficient combustion process, a suboptimal molar [NH_4NO_3/$acac^-$] = 1 ratio precursor was analyzed to clarify the subsequent decomposition steps I, II and III (see Figure 4a and 4b). In the DTA plot, it was already observed that an endothermic phenomenon (II) occurs after the mixed combustion and evaporation step (I). The FTIR spectrum at 220 °C (Figure 5b) demonstrates that for both the 2 mm and the 63 µm size fractions the release of NO_2 is present, originating from excess NH_4NO_3 decomposition and subsequent evaporation (reaction scheme 2 and 3). The endothermic signal corresponding to NH_4NO_3 evaporation is also apparent in a nitrogen atmosphere (Figure S3).

$$NH_4NO_3 \rightarrow NH_3 + HNO_3 \quad (2)$$

$$HNO_3 \rightarrow \frac{1}{2}H_2O + NO_2 + \frac{1}{4}O_2 \quad (3)$$

From these observations it can be concluded that nitrates which are not involved in the combustion reaction are partially removed by NH_4NO_3 decomposition and subsequent evaporation of NO_2. This correlates well with the endothermic signal observed in the DTA measurement [2]. After reaching a temperature of 235 °C, a notable difference between the spectra of the 2 mm and 63 µm size fractions is emerging (Figure 5c). Whereas the spectrum of the 2 mm size fraction mainly indicates continued NO_2 and H_2O evaporation, the spectrum of the 63 µm fraction points toward the oxidative reaction of the residual carbon fragments with the remaining nitrates, resulting in CO_2 evolution and signals around 2220 cm^{-1} and 1285 cm^{-1} become clear, evidencing N_2O formation. In addition, signals corresponding to NO_2 as discussed above are still present, which leads to the conclusion that for the small size fraction, a mixed process (both nitrate evaporation and residual fuel oxidation) is happening. This is probably due to the small temperature difference (15 °C) between (II) and (III) (Figure 4a) and both NH_4NO_3 degradation mechanisms occur simultaneously in a similar temperature interval. So in order to optimize the oxidizer/fuel ratio in future studies, the volatility of both components has to be taken into account.

From the first mass loss step (I) it becomes apparent that the oxidative removal of acetylacetonate fuel is considerably lower for the 63 µm fraction and the major weight loss can be assigned to acetylacetone evaporation (figure 4a, 4b and 5a). However, based on the ESI-MS measurements (Figure 3), not all the acetylacetonate ligands are liberated by the ligand exchange, leaving some $acac^-$ ions behind which are not able to evaporate easily, thus resulting in residual organic species in the sample. Combined with the lack of reaction with the present nitrates, more unburned carbon fragments might be available for the oxidative reaction at 240 °C in which the nitrates follow reaction scheme 4 [2]. The ammonium nitrate decomposition at 240 °C (vide infra)

can be associated with an exothermic signal in the DTA measurement (Figure 4b, (III)), according to the following equation:

$$NH_4NO_3 \rightarrow N_2O + 2\,H_2O \quad (4)$$

At higher temperatures, the release of water and ammonia becomes more prominent, reaching a maximum around 270 °C in both TG-FTIR and TG-MS spectra, applying a heating rate of 10 °C/min (Figure S6). This is an indication for the presence of water and ammonia molecules incorporated in the crystal structure after the combustion process took place ($NH_3(MoO_3)_3$ and MoO_3 x $0.55H_2O$, Figure 9) and partly explains the slightly decreasing baseline in Figure 4a. Eventually, residual carbon is removed from the sample at temperatures exceeding 350 °C as a significant increase in the CO_2 signal is observed. This elevated CO_2 signal is far more prominent for the small 63 µm fraction than for the 2 mm fraction, opposing the expectation that the higher specific surface area of the 63 µm fraction is beneficial for the removal of organics because of the higher contact area with oxygen present in the ambient atmosphere. So, the reverse trend indicates a more efficient removal of organics in case of a pronounced combustion reaction. Moreover, differential thermal analysis (DTA) results indicate a distinguishable weight loss after 400 °C for the 63 µm size fraction, whereas this weight loss is less pronounced for the 2 mm fraction (Figure S9). Moreover, this trend is also observed for systems with an oxidizer/fuel ratio of 0.5 (TG-FTIR data, Figure S10). Since a distinct combustion step is missing for small size fractions, it is plausible that more carbon fragments remain which can only be removed oxidatively in this high temperature range.

As stated before, a combustion reaction requires a limited surface to volume ratio to precede the Hacac fuel evaporation. Extrapolation of the observed reaction mechanism to nanoscale films implies that precursor decomposition via a thermal runaway reaction is far from evident, as confirmed by TGA performed on a film (Figure 6). Because of the large surface area compared to the film volume (mean thickness of approximately 0.31 micron, Figure S1), the acetylacetone evaporation is shifted to even lower temperatures leaving almost no fuel for combustion (Figure 8). The TGA profile of the film also shows a gradual mass loss starting at 150 °C, in contrast to the typical combustion profile. Moreover the residual mass fraction of the film is far too high, most likely due to acetylacetone evaporation during the hotplate step at 60-80 °C and during spin coating causing supplementary evaporation prior to analysis. Bearing in mind the fact that no thermal runaway reaction is observed for small size fractions and the primal weight loss step is dominated by evaporation, the TGA on film adds to the conclusion that no combustion reaction occurs at the given experimental parameters.

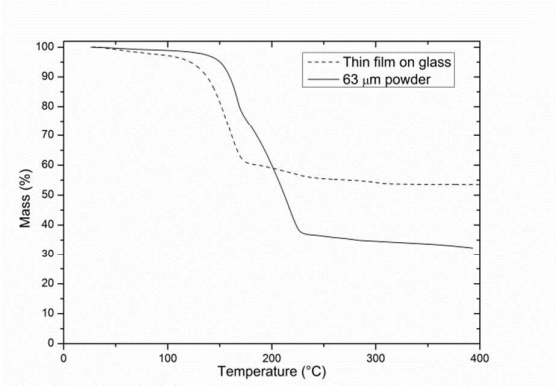

Figure 6. TG analysis on a sub 63 μm powder fraction and precursor film coated glass substrate. The total mass of the substrate coverage is 0.175 mg. Precursor has [NO_3^-/$acac^-$] ratio of 1, heating rate = 10 °C/min.

C. Heating rate influence on films

From the previous section, it became clear that fuel evaporation is the main weight loss pathway in films. However, by increasing the heating rate, the time span of the acetylacetone evaporation in the temperature range in which combustion may occur can be limited, which leaves more fuel available for the reaction with nitrates. If the contribution of this reaction becomes significant enough to induce self-heating, the autocombustion reaction sets in. This combustion on film is extremely tedious to study as it requires TGA on films and very high heating rates, which are technically unfeasible. In this section, the influence of the heating rate on the resulting film is investigated as a means to support the aforementioned hypothesis.

TGA measurements on spin coated films with various heating rates were performed. The online recorded mass fragments of the released gasses, analyzed by an online coupling with a mass spectrometer, showed a pronounced increase in m/z 44 (CO_2^+) when the heating rate is increased, which can be expected as more ions are evolving in a shorter time span. The increase in ion current is compared with m/z 42, corresponding to the $OCCH_2^+$ ion which can only be formed by alfa cleavage of Hacac and shows no spectral overlap with m/z 44 due to resolution issues, as is the case for m/z 43. At a heating rate of 60 °C/min, an elevated CO_2 release is observed in the temperature range of 150–400 °C. This increased signal might be due to the prolonged residence time of the evolved gasses in the TG-MS interface relative to the fast heating rate, and the elongated time for MS spectrum collection (9 s) compared to the heating rate, resulting in fewer data points. From Figure 7, it can be deduced that the increase of m/z 44 is proportionally more significant compared to m/z 42 at higher heating rates. It can be concluded that by increasing the heating rate, more CO_2 evolution seems to occur pointing to a

promotion of the oxidative (combustion-related) decomposition. This can be a supplementary explanation for the proportional increase of the CO_2 signal, apart from measurement setup effects.

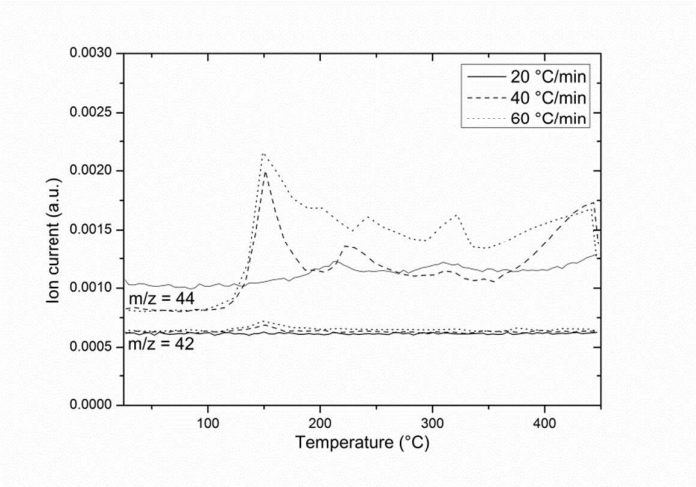

Figure 7. m/z 42 and m/z 44 ion currents as a function of TG sample temperature using various heating rates (20-40-60 °C/min), in which m/z 42 represents the $OCCH_2^+$ ion originating from Hacac evaporation, and m/z 44 is the CO_2 signal indicative of oxidative decomposition.

Besides the effect of the heating rate on the evolving gasses, the composition of the layers differs as well after thermal treatment. In Figure 8, the grazing incidence attenuated total reflection (GATR-FTIR) spectra of two MoO_x layers deposited on Si/SiO_2 native oxide substrates from the same precursor solution (0.1 M, oxidizer/fuel = 1) are presented, both treated at a maximum temperature of 225 °C. However, one substrate had a gradual hotplate treatment, in which the temperature was increased by 10 °C/min according to a routine TG measurement, while the other substrate was subjected to a sudden temperature increase from 80 to 225 °C. In a realistic process, the MoO_3 layers are spin coated on ITO coated substrates, followed by a hotplate treatment to dry the films and remove the organics in the precursor solution. Typically, two hotplate steps are applied: a 2 minute step at 60–80 °C and a two minute step at 200–300 °C. Hence, the heating rate is very high (over 100 °C in a few seconds), impossible to mimic in commercially available TGA setups. The film subjected to the gradual hotplate treatment contained more residual organics as indicated by absorbance peaks at 1695 cm^{-1} and 1601 cm^{-1} assigned to remaining acetylacetonate, pointing to the absence of combustion and a changing oxidizer/fuel ratio by means of evaporation. The most obvious differences can be found in the low wavelength range, with distinct signals at 977 cm^{-1} (s) and 898 cm^{-1} (vs) in the hotplate treated sample which can be assigned to ν(O=Mo) and ν(OMo_2) stretch vibrations, respectively [54]. The bands are slightly shifted compared to the orthorhombic MoO_3

structure, suggesting the presence of NH_3 and H_2O in the crystal structure distorting the Mo-O octahedra (confirmed by XRD [55], Figure 9). The increased absorbance at 702 cm^{-1} and the continued signal above 3500 cm^{-1} can be ascribed to the presence of amorphous MoO_x secondary phases containing water, as regularly observed in literature [20]. Finally, the signal at 1380 cm^{-1} is assigned to the presence of excess nitrates, which are not evaporated completely after 2 minutes at 225 °C. The ATR spectrum of the gradual temperature treatment shows less distinct signals in the region below 1000 cm^{-1}, prognosticating the presence of a layer of lower crystallinity (more evaporation, changing oxidizer/fuel ratio, no combustion, difference in crystallinity confirmed by Figure S11). From this analysis, it can be concluded that a higher heating rate leads to a reduced organic content and promotes crystallization. Calcination at slightly higher temperatures (300 °C for 1 hour) will remove the incorporated water and ammonia resulting in a MoO_3 layer with possible application in OPVs (Figure 9). After post-calcination, the organic content is negligible, demonstrated by the corresponding GATR-FTIR spectrum (Figure S12).

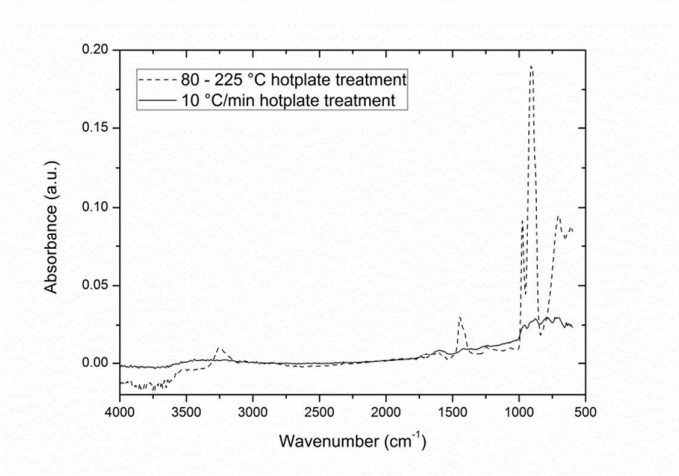

Figure 8. GATR-FTIR spectra of MoO_x layers treated at 225 °C, after 4 subsequent deposition cycles from 0.1 M precursor on Si/SiO_2 native oxide substrate. The dashed line spectrum describes the MoO_x hotplate processing corresponding to a high heating rate, the full line spectrum shows the same layer subjected to a gradual heating program.

MoO_3 layers

The previous sections indisputably demonstrated the influence of the surface to volume ratio, nitrate content and heating rate on the formation of molybdenum oxide from the considered precursor system. Bearing these findings in mind, functional OPV interfacial layers are obtained using the [oxidizer/fuel] = 1 and 0.5 ratio [ammonium nitrate/acetylacetonate] precursors. All films are synthesized using 2 hotplate steps (at 80 °C and a

specified second step between 200 and 250 °C) and a post calcination step (300 °C) to obtain the desired o-MoO_3 phase. At temperatures lower than 225 °C, crystalline Mo containing phases are formed. However, due to the strong XRD peak overlap, the exact crystal structure could not be distinguished unambiguously and two possible phases are proposed (Figure 9). Both phases consist of a layered structure of distorted Mo-O octahedra with NH_3 and H_2O molecules in the voids formed by the terminal oxygen atoms [55, 56]. The presence of both phases is plausible as TG-FTIR analysis indicates H_2O and NH_3 evolution between 225 and 300 °C (Figure S10), resulting in o-MoO_3 after a post calcination step at 300 °C for 1 hour. In systems without nitrates, only noisy X-ray diffractograms could be obtained in which the phase could not be unambiguously identified because of the extensive array of possible MoO_x phases.

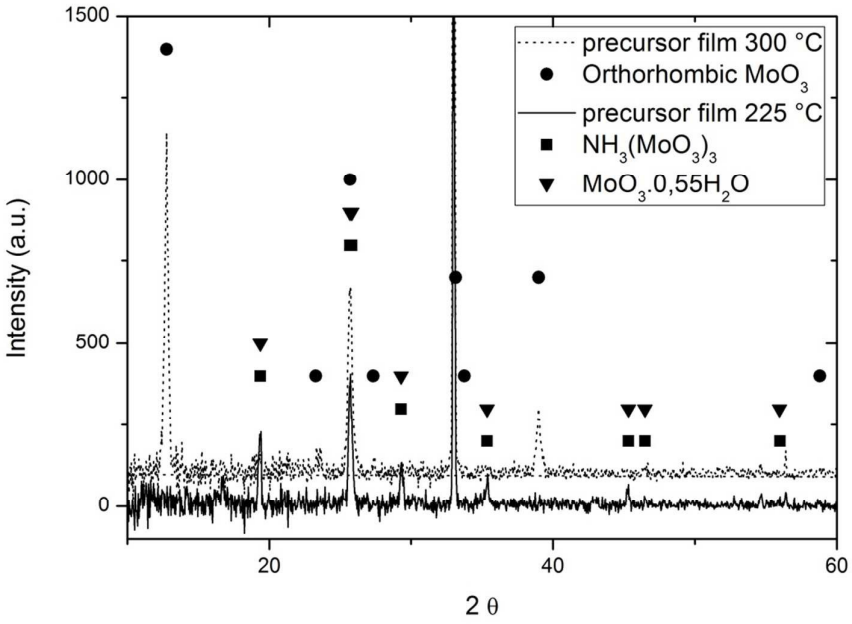

Figure 9. XRD patterns of MoO_x layers on Si/SiO_2 native oxide substrates (intense substrate peak at 2θ = 33°). The o-MoO_3 phase is formed during the post calcination at 300 °C as shown in Figure 11. JCPDS: o-MoO_3: 005-0508, MoO_3 x 0.55H_2O: 048-0399, $NH_3(MoO_3)_3$: 039-0035

An important trend in film formation can be discovered when the film morphology is investigated after deposition from different molybdenum precursor concentrations, 0.05 M, 0.1 M, 0.2 M and 0.3 M, on ITO covered glass substrates. Higher precursor concentrations result in thicker films with more internal volume. The number of deposition cycles is varied as a function of the precursor concentration to deposit a comparable amount of material. From the SEM images in Figure 10, it can be seen that 0.05 M precursor films are more

smooth and homogeneous, whereas the films deposited from more concentrated solutions result in a strong gas evolution, affecting the film morphology. Keeping the insights on surface-volume ratio in mind, it can be postulated that the gas evolution in the thicker films has a larger combustion contribution resulting in a sudden film blow-up. The growing inhomogeneity reduces the film transparency, favoring the use of low concentration precursors. The reported transparency values are corrected for the background (subtraction of glass and ITO layer). To confirm that the decreased transparency could be attributed solely to a morphological effect, multiple layers of the diluted precursors were deposited and inspected with cross section SEM to ensure similar MoO_3 film thicknesses (1 layer of 0.30 M, 2 layers of 0.20 M, 4 layers of 0.10 M and 6 layers of 0.05 M). However, the layers fabricated from the 0.05 M precursor are not perfect and still contain pin-holes and surface roughness which can cut the OPV performance of the layer (Figure S13). Based on transparency measurements on 4 layers of the 0.10 M MoO_3 precursors, Tauc plots (Figure S14) were constructed yielding values of 2.95 eV and 3.64 eV for the indirect and direct band gap respectively, which is in acceptable agreement with both calculated values (2.81 eV, indirect band gap [57]) and several experimental determinations depending on the method of preparation and the applied fitting model [58].

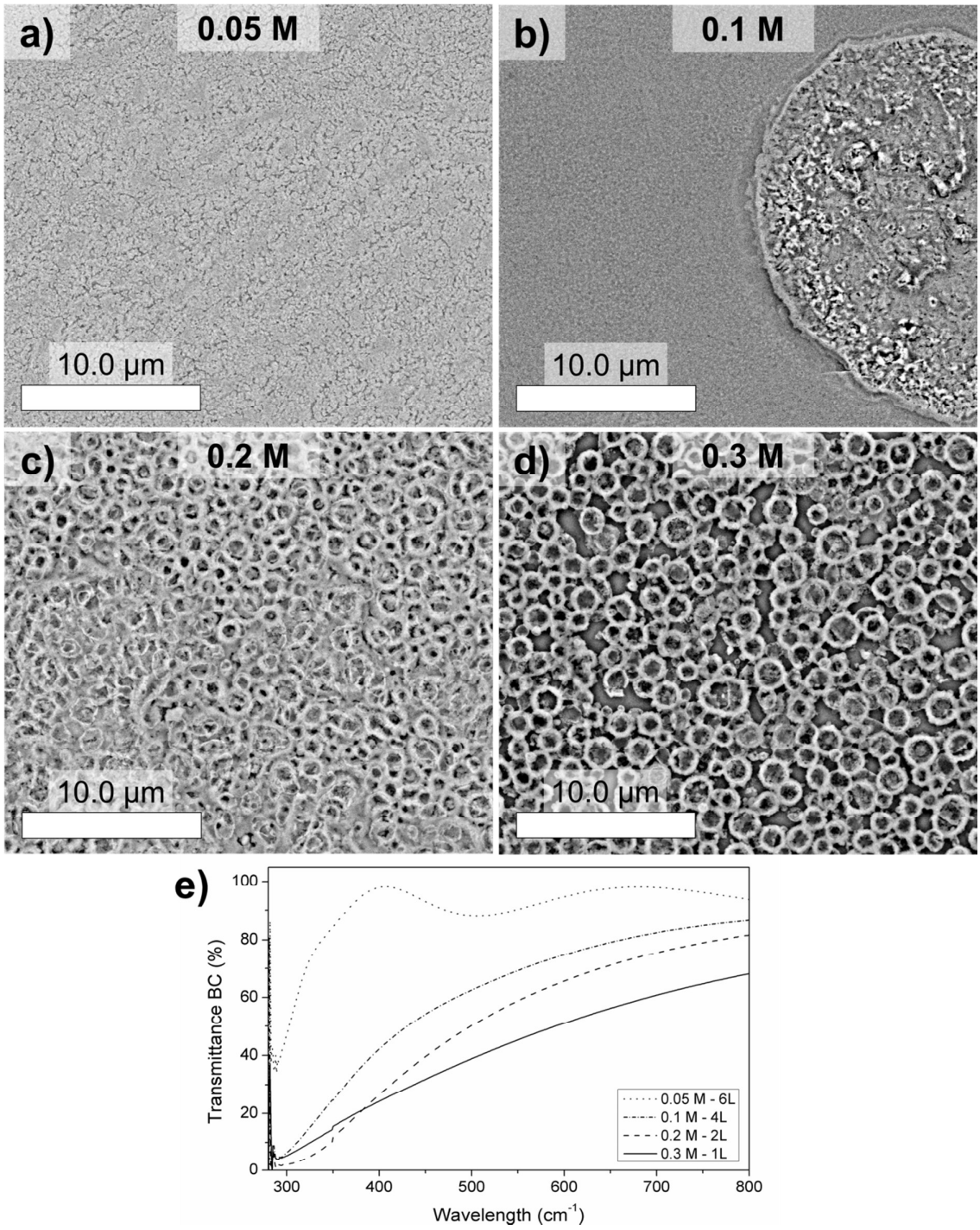

Figure 10. SEM images (magnification 10000 X) of MoO_3 layers deposited from different precursor concentrations(a-d) indicating a changing morphology and their influence on the transparency in UV-Vis (e).

Another remarkable fact is the influence of the second hotplate step on the layer morphology and crystallinity. The difference in temperature between the subsequent hotplate steps at 80 °C and in the range of 200–300 °C

implies a different heating rate. Samples subjected to a temperature program of 80 °C and 300 °C hotplate steps will experience a steeper heating rate compared to samples treated at 80 °C and 200 °C consecutively. All the following samples had a post calcination of 2 hours at 300 °C. In the Raman spectra (Figure S15), no features corresponding to crystalline o-MoO_3 can be perceived for the 80–200 °C hotplate program. When the second hotplate temperature is increased to 300 °C, small signals at 995 cm^{-1} and 820 cm^{-1} can be observed, corresponding to terminal ν(O=Mo) and ν(OMo_2) stretching respectively [45, 54]. This experiment suggests that the crystallinity is enhanced by an increased temperature difference between both hotplate steps, as the Raman signals observed with a 80-300 °C hotplate treatment match the o-MoO_3 phase. A similar evolution can be noticed in the corresponding XRD patterns of MoO_x layers on ITO. When a hotplate temperature of 200 °C is applied, no crystalline o-MoO_3 is observed, in contrast to a second stage hotplate temperatures at 250 °C and 300 °C (see Figure 11).

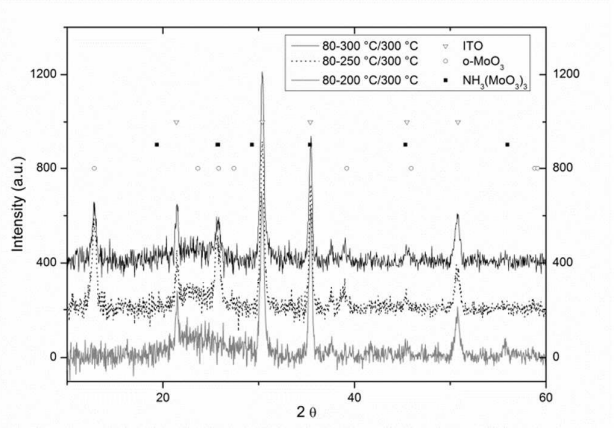

Figure 11. XRD patterns of MoO_3 layers on ITO substrates. The second hotplate step (2 minutes) is varied, which clearly influences the crystallinity of the resulting layers

After exploring various deposition parameters, the optimal conditions were selected in order to test the hole conducting properties of the MoO_3 layers indirectly via OPV characterization. Because of the morphological imperfections and the limited thickness of the layer, measuring the in-plane conductivity would have been a tedious experiment (on a conductive ITO layer). Organic photovoltaic cells were produced conform the state of the art (see experimental section), based on the PCDTBT:PC_{70}BM active layer blend [59]. Molybdenum precursors (0.05 M and 0.10 M) which proved to yield the most homogeneous morphology were applied on the ITO substrates by spin coating (differences in OPV output characteristics between both precursor concentrations were minimal). After a hotplate treatment, the films were calcined in dry air at 300 °C as a N_2 atmosphere badly affected the average power conversion efficiency (PCE) values (2.50 ± 0.37 % compared to 3.10 ± 0.28 %). The influence of the second hotplate step temperature (200-300 °C) on the OPV output seems rather limited as long

as films were finally calcined at 300 °C, which means that the mechanism of the crystallinity-increased conductivity [43] could not be confirmed in this study (no increase in J_{sc}). The thickness of the active PCDTBT:PC70BM layer was also varied between 60 and 100 nm, but had no significant consequence on the final device performance (average PCE's of 3.11 and 3.14 %, respectively). The best performing molybdenum oxide layers are summarized in Figure 12. The obtained MoO_3 interlayers are compared to a reference cell using PEDOT:PSS. The average device characteristics for a MoO_3 containing device stack annealed in dry air are: V_{oc} = 0.82 V, J_{sc} = 8.13 mA/cm^2, FF = 0.47 and PCE = 3.10 %. From the J-V curves (Figure 12) of the highest PCE stacks, it can be observed that the PEDOT:PSS layer performs better compared to MoO_3, mainly attributed to the difference in J_{sc} (9.32 versus 7.70 mA/cm^2) and FF (0.58 versus 0.55). This trend is generally recognized in all samples, keeping in mind the average values mentioned before. The reason for this small lack in performance can be attributed to the inherently limited conductivity of the MoO_3 layer and the roughness (AFM rms average roughness: 10.96 nm), which can be expected from the sudden gas evolution during the layer processing. From this study, it becomes apparent that crystalline o-MoO_3 layers have a comparable performance relative to sputtered amorphous ones in a similar stack [22], which is a strong achievement for a solution-based process. The output characteristics of the MoO_3 containing stack are in the line of expectations when compared to other studies developing solution processed MoO_3 [26, 60, 61]. The inferior J_{sc} and FF can be tackled by further improving the morphology and transparency and through the introduction of specific dopants, for which this precursor system is very suitable.

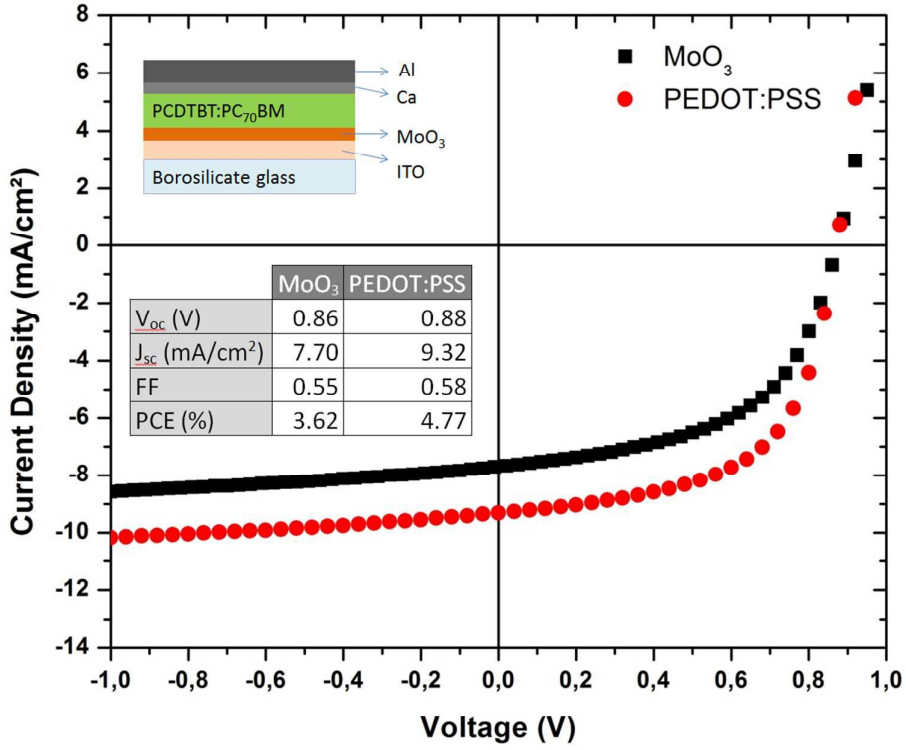

Figure 12. J-V curves of the best performing MoO_3 containing stack from a 0.05 M Mo precursor, treated on a hotplate at 80 °C and 200 °C with a 300 °C post calcination step, compared to a reference stack using a PEDOT:PSS hole transport layer.

Conclusion

In summary, various parameters influencing combustion synthesis were investigated in this work. The synthesis of a functional MoO_3 interlayer for OPV applications was used as a test case to illustrate important variables such as the oxidizer/fuel ratio, the surface to volume ratio and the heating rate effect. It was reported that the volatility of the present acetylacetone fuel affects the required oxidizer fuel ratio for optimal combustion. Furthermore, the contribution of the combustion reaction faded out on increasing the surface to volume ratio, which can be related to the balance between generated and dissipated heat, and the increased relative occurrence of acetylacetone evaporation. Moreover, the heating rate seems to have a strong influence in this process, promoting oxidative decomposition when increased. The remarkable difference between films resulting from a gradual temperature treatment and films subjected to stepwise temperature increase, together with the more significant oxidative degradation mechanism may suggest the occurrence of combustion in films in these particular process conditions. The obtained MoO_3 layers (based on GATR and XRD) were crystalline and

function well in typical OPV stacks. However, further improvement is required to outperform the conventional PEDOT:PSS hole transporting material. Because of the selected versatile precursor system, the addition of dopants, further improving the device output characteristics, can be identified as future challenge to tackle.

Acknowledgements

This research was supported by the FWO, the Research Foundation Flanders, project G041913N. C. De Dobbelaere is a post-doctoral research fellow of the Research Foundation Flanders (FWO Vlaanderen). J. Kesters acknowledges Hasselt University for his PhD scholarship. Guy Reggers and Martine Vanhamel are acknowledged for their technical support regarding the thermogravimetric analyses. Giedrius Degutis is acknowledged for the Raman measurements.

References

1. F. Deganello, G. Marcì and G. Deganello, *J. Eur. Ceram. Soc.*, 2009, **29**, 439-450.
2. S. Biamino and C. Badini, *J. Eur. Ceram Soc.*, 2004, **24**, 3021-3034.
3. T. Striker and J. A. Ruud, *J. Am. Ceram. Soc.*, 2010, **93**, 2622-2629.
4. R. Branquinho, D. Salgueiro, L. Santos, P. Barquinha, L. Pereira, R. Martins and E. Fortunato, *ACS Appl. Mater. Interfaces*, 2014, **6**, 19592-19599.
5. K. Morsi, *J. Mater. Sci.*, 2011, **47**, 68-92.
6. A. S. Mukasyan and P. Dinka, *Int. J. Self-Propag. High-Temp. Synth.*, 2007, **16**, 23-35.
7. S. Söllradl, M. Greiwe, V. J. Bukas, M. R. Buchner, M. Widenmeyer, T. Kandemir, T. Zweifel, A. Senyshyn, S. Günther, T. Nilges, A. Türler and R. Niewa, *Chem. Mater.*, 2015, **27**, 4188-4195.
8. A. S. Mukasyan, P. Epstein and P. Dinka, *Proc. Combustion Institute*, 2007, **31**, 1789-1795.
9. T. Minami and K. C. Patil, *Mater. Phys. Mech.*, 2001, **4**, 134-137.
10. Z. Yue, J. Zhou, L. Li, H. Zhang and Z. Giu, *J. Magn. Magn Mater.*, 1999, **208**, 55-60.
11. S. R. Jain, K. C. Adiga and V. R. Pai Verneker, *Combust. flame*, 1981, **40**, 71-79.
12. K. C. Patil, S. T. Aruna and T. Mimani, *Curr. Opin. Solid State Mater. Sci.*, 2002, **6**, 507-512.
13. I. Glassman and R. A. Yetter, *Combustion*, Elsevier Inc., London, 2008.
14. A. Hardy and M. K. Van Bael, *Nat. Mater.*, 2011, **10**, 340-341.
15. D. Sanchez-Rodriguez, J. Farjas, P. Roura, S. Ricart, N. Mestres, X. Obradors and T. Puig, *J. Phys. Chem. C*, 2013, **117**, 20133-20138.
16. M. G. Kim, M. G. Kanatzidis, A. Facchetti and T. J. Marks, *Nat. Mater.*, 2011, **10**, 382-388.
17. J. W. Hennek, M. G. Kim, M. G. Kanatzidis, A. Facchetti and T. J. Marks, *J. Am. Chem. Soc.*, 2012, **134**, 9593-9596.
18. Y. Narendar and G. L. Messing, *J. Am. Ceram. Soc.*, 1997, **80**, 914-925.
19. S. Esiner, T. Bus, M. M. Wienk, K. Hermans and R. A. J. Janssen, *Adv. Energy Mater.*, 2013, **3**, 1013-1017.
20. J. J. Jasieniak, J. Seifter, J. Jo, T. Mates and A. J. Heeger, *Adv. Funct. Mater.*, 2012, **22**, 2594-2605.
21. J. Meyer, S. Hamwi, M. Kroger, W. Kowalsky, T. Riedl and A. Kahn, *Adv. Mater.*, 2012, **24**, 5408-5427.
22. J. Griffin, D. C. Watters, H. Yi, A. Iraqi, D. Lidzey and A. R. Buckley, *Adv. Energy Mater.*, 2013, **3**, 903-908.
23. S. Chen, J. R. Manders, S.-W. Tsang and F. So, *J. Mater. Chem.*, 2012, **22**, 24202.
24. H. Choi, B. Kim, M. J. Ko, D. K. Lee, H. S. H. Kim and K. Kim, *Org. Electron.*, 2012, **13**, 959-968
25. K. Zilberberg, S. Trost, J. Meyer, A. Kahn, A. Behrendt, D. Lützenkirchen-Hecht, R. Frahm and T. Riedl, *Adv. Funct. Mater.*, 2011, **21**, 4776-4783.

26. P. Qin, G. Fang, W. Ke, F. Cheng, Q. Zheng, J. Wan, H. Lei and X. Zhao, *J. Mater. Chem. A*, 2014, **2**, 2742.
27. M. J. Beliatis, K. K. Gandhi, L. J. Rozanski, R. Rhodes, L. McCafferty, M. R. Alenezi, A. S. Alshammari, C. A. Mills, K. D. Jayawardena, S. J. Henley and S. R. Silva, *Adv. Mater.*, 2014, **26**, 2078-2083.
28. C. Girotto, E. Voroshazi, D. Cheyns, P. Heremans and B. P. Rand, *ACS Appl. Mater. Interfaces.*, 2011, **3**, 3244-3247.
29. T. Stubhan, T. Ameri, M. Salinas, J. Krantz, F. Machui, M. Halik and C. J. Brabec, *Appl. Phys. Lett.*, 2011, **98**, 253308.
30. M. Kröger, S. Hamwi, J. Meyer, T. Riedl, W. Kowalsky and A. Kahn, *Appl. Phys. Lett.*, 2009, **95**, 123301.
31. Y. Sun, C. J. Takacs, S. R. Cowan, J. H. Seo, X. Gong, A. Roy and A. J. Heeger, *Adv. Mater.*, 2011, **23**, 2226-2230.
32. E. Ramírez-Meneses, F. Cervantes-Sodi, M. A. Hernández-Pérez, J. L. Vázquez-Olavarrieta, A. Aguilar-Morales and R. Martínez-Guerrero, *ide@s CONCYTEG*, 2012, **7**, 1083-1090.
33. A. Siokou, G. Leftheriotis, S. Papaefthimiou and P. Yanoulis, *Surf. Sci.*, 2001, 294-299.
34. O. M. Hussain, K. Srinivasa Rao, K. V. Madhuri, C. V. Ramana, B. S. Naidu, S. Pai, J. John and R. Pinto, *Appl. Phys. A*, 2002, **75**, 417-422.
35. T. M. McEvoy and K. J. Stevenson, *Anal. Chim. Acta*, 2003, **496**, 39-51.
36. J. Meyer, R. Khalandovsky, P. Gorrn and A. Kahn, *Adv. Mater.*, 2011, **23**, 70-73.
37. B. J. Tremolet de Villers, R. C. I. MacKenzie, J. J. Jasieniak, N. D. Treat and M. L. Chabinyc, *Adv. Energy Mater.*, 2014, **4**, 1-10.
38. R. W. Schwartz, T. Schneller and R. Waser, *C. R. Chim.*, 2004, **7**, 433-461.
39. I. Hancox, L. A. Rochford, D. Clare, M. Walker, J. J. Mudd, P. Sullivan, S. Schumann, C. F. McConville and T. S. Jones, *J. Phys. Chem. C*, 2013, **117**, 49-57.
40. N. Y. Ko, S. B. Park and Y. C. Kang, *Chem. Asian J.*, 2014, **9**, 1011-1015.
41. D. Parviz, M. Kazemeini, A. M. Rashidi and K. Jafari Jozani, *J. Nanopart. Res.*, 2009, **12**, 1509-1521.
42. L. Chibane, M. S. Belkaid, M. Pasquinelli, H. Derbal-Habak, J. J. Simon, D. Hocine and O. Boudia, presented in part at the International Conference on Renewable Energies and Power Quality, Santiago de Compostela (Spain), 2012.
43. D. Cheyns, B. Kam, K. Vasseur, P. Heremans and B. P. Rand, *J. Appl. Phys.*, 2013, **113**, 043109.
44. M. Kovendhan, D. P. Joseph, P. Manimuthu, S. Sambasivam, S. N. Karthick, K. Vijayarangamuthu, A. Sendilkumar, K. Asokan, H. J. Kim, B. C. Choi, C. Venkateswaran and R. Mohan, *Appl. Surf. Sci.*, 2013, **284**, 624-633.
45. K. Ajito, L. A. Nagahara, D. A. Tryk, K. Hashimoto and A. Fujishima, *J. Phys. Chem.*, 1995, **99**, 16383-16388.
46. R. Grybos, A. Samotus, N. Popova and K. Bogolitsyn, *Transition Met. Chem.*, 1997, **22**, 61-64.
47. K. C. Patil, M. S. Hedge, T. Rattan and S. T. Aruna, *Chemistry of nanocrystalline oxide materials*, World Scientific, Singapore, 2008.
48. A. Civera, M. Pavese, G. Saracco and V. Specchia, *Catalysis Today*, 2003, **83**, 199-211.
49. T. Minami, *J. Alloy Compd.*, 2001, **315**, 123-128.
50. V. C. Sousa, A. M. Segadaes, M. R. Morelli and R. H. G. A. Kiminami, *Int. J. Inorg. Mater.*, 1999, **1**, 235-241.
51. W. Wen and J.-M. Wu, *RSC Adv.*, 2014, **4**, 58090-58100.
52. M. G. Kim, J. W. Hennek, H. S. Kim, M. G. Kanatzidis, A. Facchetti and T. J. Marks, *J. Am. Chem. Soc.*, 2012, **134**, 11583-11593.
53. H. C. Yi and J. J. Moore, *J. Mater. Sci.*, 1990, **25**, 1159-1168.
54. L. Seguin, M. Figlarz, R. Cavagnat and J.-C. Lassègues, *Spectrochim. Acta A*, 1995, **51**, 1323-1344.
55. J. L. Garin and J. M. Blanc, *J. Solid State Chem.*, 1985, 98-102.
56. J. Guo, P. Zavalij and M. Whittingham, *Eur. J. Solid State Inorg. Chem.*, 1994, **31**, 883.
57. A. H. Reshak, *RSC Adv.*, 2015, **5**, 22044-22052.
58. M. F. Al-Kuhaili, S. M. A. Durrani, I. A. Bakhtiari and A. M. Al-Shukri, *Opt. Commun.*, 2010, **283**, 2857-2862.
59. J. Kesters, T. Ghoos, H. Penxten, J. Drijkoningen, T. Vangerven, D. M. Lyons, B. Verreet, T. Aernouts, L. Lutsen, D. Vanderzande, J. Manca and W. Maes, *Adv. Energy Mater.*, 2013, 1180–1185.
60. K. Zilberberg, H. Gharbi, A. Behrendt, S. Trost and T. Riedl, *ACS Appl. Mater. Interfaces*, 2012, **4**, 1164-1168.
61. S. Kato, R. Ishikawa, Y. Kubo, H. Shirai and K. Ueno, *Jpn. J. Appl. Phys.*, 2011, **50**, 1-5.